Performance of a Compensating Lead/Plastic-Scintillator Tile/Fiber Calorimeter

S. Uozumi [f,1], T. Asakawa [f,2], J. P. Done [e,3], Y. Fujii [a], K. Furukawa [d,4], K. Hara [f], T. Ishizaki [f,5], S. Kaga [d,6], F. Kajino [c], T. Kamon [e], N. Kanaya [b], J. Kanzaki [a], K. Kawagoe [b], S. Kim [f], A. Miyajima [d], A. Nakagawa [f,7], M. Nozaki [b], R. Oishi [f], T. Ota [f,8], K. Sendai [a], Y. Sugimoto [b,9], Y. Sugimoto [a], T. Suzuki [f], H. Takeda [b], T. Takeshita [d], A. Takeuchi [b,10], T. Toeda [d,11], Y. Yamada [c]

[a] *Institute of Particle and Nuclear Studies, High Energy Accelerator Research Organization (KEK), Tsukuba, Ibaraki 305-0801, Japan*

[b] *Department of Physics, Kobe University, Kobe, Hyogo 657-8501, Japan*

[c] *Department of Physics, Konan University, Kobe, Hyogo 658-8501, Japan*

[d] *Department of Physics, Shinshu University, Matsumoto, Nagano 390-8621, Japan*

[e] *Department of Physics, Texas A&M University, College Station TX 77843-4242, USA*

[f] *Institute of Physics, University of Tsukuba, Tsukuba, Ibaraki 305-8571, Japan*

Abstract

We have measured performance of a lead/plastic scintillator sampling calorimeter in two separate beam tests at low ($1 \sim 4$ GeV) and high ($10 \sim 200$ GeV) energies. The calorimeter is composed of 8-mm-thick lead plates and 2-mm-thick plastic scintillator plates for hardware compensation, where responses to electromagnetic and hadronic showers of the same energy are identical. We find the linearity to be better than 1% in the energy range between 2 GeV and 150 GeV for both pions and electrons. The energy resolutions are obtained to be $(46.7 \pm 0.6)\%/\sqrt{E} \oplus (0.9 \pm 0.9)\%$ for pions, where the energy E is given in GeV. The response ratio of electromagnetic showers to hadronic showers is measured to be 1.04 ± 0.01 at low energies, and 0.99 ± 0.01 at high energies.

Key words: calorimeter, hadron calorimeter, compensation, tile/fiber, e/π
PACS: 29.40.Mc, 29.40.Vj

---

1 Introduction

In order to perform precise measurements of the Standard Model as well as studies of new physics, R&D's for e^+e^- linear colliders are extensively carried out in major high-energy physics institutes in the world. The linear colliders will provide clear experiments owing to their well-defined elementary processes. In order to fully take advantage of the clearness, detectors of the most excellent performance are indispensable [1]. For the calorimetry, in order to distinguish W and Z bosons using their reconstructed 2-jet masses, the following energy resolutions are required [1];

$$\sigma_E/E = 40\%/\sqrt{E} \oplus 2\% \quad \text{for hadrons, and}$$

$$\sigma_E/E = 15\%/\sqrt{E} \oplus 1\% \quad \text{for electrons and photons}$$

where the energy E is given in GeV, and the symbol $\oplus$ denotes a quadratic sum.

The required hadron energy resolution can only be achieved by calorimetry with compensation; either with hardware compensation or with software compensation. We adopt the hardware compensation with lead absorber and plastic scintillator as a primary candidate from the viewpoint of design simplicity, production cost, and detector density. In addition to the excellent hadron energy resolution, the hardware compensation provides very good features such as a Gaussian pulse-height distribution and an excellent linearity. Low photon yield, on the other hand, shall not be a problem for hadron calorimetry.

[1] Corresponding author. High Energy Physics Laboratory, Institute of Physics, University of Tsukuba, 1-1-1 Tenno-dai, Tsukuba-shi, Ibaraki-ken 305-8571, Japan. telephone : +81-298-53-4270, fax : +81-298-53-4491, e-mail : satoru@hepsg1.px.tsukuba.ac.jp
[2] present address : Yokogawa-Denki, Kofu, Yamanashi 400-0057, Japan
[3] present address : Raytheon, 299 N. Euclid Ave. Ste.#500, Pasadena, CA 91101, USA
[4] present address : Nidec Copal Corp., Kohriyama, Fukushima 963-8637, Japan
[5] present address : Fujitsu Limited, Akiruno, Tokyo 197-0833, Japan
[6] present address : Toyota Techno Service Co., Toyota, Aichi 470-1201, Japan
[7] present address : Media Technology Co.,Ltd., Shibuya-ku, Tokyo 151-0053, Japan
[8] present address : Nintendo Co.Ltd., Minami-ku, Kyoto 601-8501, Japan
[9] present address : Motorola Japan Ltd., Minato-ku, Tokyo 106-8573, Japan
[10] present address : Fujitsu Limited, Nakahara-ku, Kawasaki, Kanagawa 211-8588, Japan
[11] present address : Department of Physics, Nagoya University, Nagoya, Aichi 464-8602, Japan

In our previous paper, we have presented a configuration which achieves precise compensation [2]. Based on the results, we have built a tile/fiber hadron calorimeter module and carried out a series of tests with low-energy beams ($1 \sim 4$ GeV) at High Energy Accelerator Research Organization (KEK) and with high-energy beams ($10 \sim 200$ GeV) at Fermi National Accelerator Laboratory (FNAL).

In this paper we report the beam test results of the compensating tile/fiber hadron calorimeter. In section 2, the test module design is described. In section 3, outlines of the two beam tests are described. We present the results of the beam tests in section 4. Conclusions are given in section 5.

2 Calorimeter Module

2.1 Module Design

The calorimeter module is a sampling calorimeter composed of 8-mm-thick lead plates and 2-mm-thick plastic scintillator plates with a transverse size of 1 m $\times$ 1 m. The module has a hanging-file structure, where both lead and plastic scintillator plates are hung over a pair of supporting beams as shown in Fig. 1. It should be noted that the volume ratio of lead to plastic scintillator plates is 8:2, which is close to the exact compensation ratio of 9:2 measured in Ref. [2]. This configuration was expected to achieve hadron energy resolution of $40\%/\sqrt{E}$ by extrapolating the result of $44\%/\sqrt{E}$ for a calorimeter with 10-mm-thick lead plates and 2.5-mm-thick plastic scintillator plates [3].

The calorimeter module consists of a front part (FCAL) and a rear part (RCAL). The configuration of FCAL is shown in Fig. 2. It is a tile/fiber calorimeter with a 5×5 tower structure. A tower is further divided into 4 blocks along the longitudinal direction. Each block has 20 layers of lead plates, scintillator tiles, and 2-mm-thick acryl plates located at the downstream-side of the tiles, resulting in a thickness of 1.04 λ_I (nuclear interaction length). One block corresponds to one photomultiplier tube (PMT) for readout. Twenty-five blocks at the same longitudinal position makes one section.

Figure 3 shows the optical readout scheme of the scintillator tile assembly in FCAL. Twenty-five scintillator tiles are arranged on a fiber-routing acryl plate to form the 5×5 tower structure, and sandwiched with white PET films. Scintillator tiles are made of Kuraray SCSN-38 with a size of 20 cm $\times$ 20 cm $\times$ 2 mm-thick. Four sides of the tiles are painted white with TiO_2-based emulsion. They have a σ-shaped groove with a key-hole cross-section, where a 1-mm-ϕ wavelength shifter (WLS) fiber with Y11-die is embedded as shown in Fig. 4. The WLS fiber is connected to a clear fiber at the exit from the tile groove with heat-splicing method [4]. The clear fibers are connected to another set of clear-fiber bundles which runs to PMTs. The clear-fiber bundles are re-arranged so that 20 fibers from one block are connected to a PMT. The photoelectron yield is estimated to be 83 photoelectrons/GeV from our result at a bench test. This has an effect to slightly deteriorate the hadron energy resolution from $40\%/\sqrt{E}$ to $41\%/\sqrt{E}$.

In the low-energy beam test at KEK (T411), conventional PMTs (Hamamatsu H1949) were used for all blocks. In the high-energy beam test at FNAL (T912), on the other hand, fine-mesh PMTs (Hamamatsu H6614-01) were used for central blocks in the sections 1 and 2 to avoid saturation of PMT gains in the case that high-energy electrons are incident.

RCAL does not have a tower structure. The configuration of RCAL is shown in Fig. 5. Each RCAL scintillator plate has six straight grooves with a key-hole cross-section, where WLS fibers are embedded. Each end of a WLS fiber is spliced to a clear fiber at the exit from a groove. Clear fibers from each side of five successive scintillator plates are bundled to make a superlayer, and run to PMTs.

In the low-energy beam test, RCAL had two superlayers, resulting in the total thickness of the calorimeter (FCAL+RCAL) of 4.59 λ_I. In the high-energy beam test, RCAL had 10 superlayers. The most downstream RCAL superlayer did not have the lead absorber plates to be used for muon tagging and leak-veto, resulting in a total calorimeter thickness of 6.37 λ_I.

2.2 Effect of Acryl Plates

In order to examine effects of fiber-routing acryl plates on compensation and energy resolution, calorimeter performance was measured in a series of generic beam tests at KEK before designing the tile/fiber module. The setup, analysis method, and systematic errors are described in detail in Ref. [2]. The module was totally a straight-groove module as shown in Fig. 5.

Following three configurations were tested:

- no acryl plates (lead and scintillator plates only) are used;
- an acryl plate is placed upstream-side of every scintillator plate;
- an acryl plate is placed downstream-side of every scintillator plate.

Thicknesses of lead plates, plastic scintillator plates, and acryl plates were 8, 2, and 2 mm, respectively. The measured energy resolutions and e/π ratios are summarized in Table. 1. Based on this measurement, acryl plates are designed to be located on the downstream-side of the scintillator plates.

3 Beam Tests

3.1 Low-energy Beam Test at KEK (T411)

3.1.1 Setup

The T411 beam test was carried out at $\pi 2$ beamline of KEK proton synchrotron in July 1998. The beamline provides unseparated beam of momentum up to 4 GeV/c with a momentum bite of 1% in terms of a full width at half maximum (FWHM).

The setup is schematically shown in Fig. 6. Three trigger scintillation counters (T1$\sim$T3) with a cross-section of 4 cm $\times$ 4 cm, two gas Cherenkov counters (C1 and C2) for electron identification, and four drift chambers (D1$\sim$D4) for particle tracking were installed on the beamline. Another scintillation counter (M1) was located downstream of the calorimeter module for muon tagging. In order to trigger muons penetrating each tower, the calorimeter module was sandwiched by a pair of muon matrix counters (MX1 and MX2).

Four sets of triggers were used for data taking. One was an inclusive trigger, a coincidence of the three trigger counters T1&T2&T3. An electron trigger was built as a coincidence of the trigger counters and the Cherenkov counters as T1&T2&T3&C1&C2. Two muon triggers, T1&T2&T3&M1 and MX1&MX2, were used for calibration purpose. In the case of MX1&MX2, the beam was defocused to deliver particles to all towers. Further particle identification was performed offline. Signals from the beamline devices and the calorimeter module were read with a PC-based CAMAC system.

Data were taken for momenta of 1, 2, 3 and 4 GeV/c for inclusive and for electron triggers. Muon triggers were used to take data for gain calibration at 2 GeV/c.

3.1.2 Gain Calibration

In order to calibrate the gains of each FCAL block in the central tower and of the RCAL superlayers, events with the muon trigger T1&T2&T3&M1 are used, while events with the muon trigger MX1&MX2 are used for off-center FCAL blocks.

The following cuts are applied to select events in which one single muon penetrated the FCAL block to be calibrated (called target block here).

- The upstream-side muon matrix counter which covers the target block should have a signal consistent with one MIP.
- All RCAL superlayers should have a signal consistent with one MIP.
- The upstream and downstream blocks of the target block should have signals consistent with one MIP.
- The signal of any other neighboring block of the target block should be consistent with the pedestal.

Here MIP stands for a minimum-ionizing particle.
Event selection for the RCAL calibration is performed as follows.

- The FCAL signal of any block in any tower except the central tower should be consistent with the pedestal.
- The most downstream block in the central tower of FCAL should have a signal consistent with one MIP.
- The muon matrix counter at the downstream side should have a signal consistent with one MIP.
- All RCAL signals should be separated well from the pedestals.

Typical pulse-height distributions for selected events are shown in Fig. 7. The top and bottom distributions are for the tower 1 at the corner and for the tower 13 at the center, respectively. Each distribution is fitted with a Gaussian function, and the calibration constant is defined as the peak position of the fitted function. The distribution is slightly different from the Gaussian distribution at the higher-tail region. The stability of the calibration constants against the fitting range is examined by data to be about 1.4%. The fraction of pion events in the muon sample is estimated using the RCAL signals. Events which have a signal bigger than that of one MIP in each RCAL superlayer are considered as pion contamination, and the fraction is counted to be less than 0.9%.

Statistical uncertainties of the calibration constants are shown in Fig. 8. Inner 9 towers are calibrated within about 2%, while outer 16 towers have calibration uncertainties of about 4% due to low statistics caused by the profile of the defocused beam.

3.1.3 Event Selection

First of all, single-particle events are selected by requiring that all trigger counters have signals consistent with one MIP. Particles are identified using the pulse-height information of the Cherenkov counters, the muon counter, and RCAL.

Electron samples are made from electron-trigger data. Electrons are efficiently separated from other particles using the pulse height of the Cherenkov counters. To reduce a contamination due to the knock-on reaction in the Cherenkov counters, events in which sum of the RCAL signals is greater than 0.15 MIP-equivalent are further rejected. The fraction of muons and hadrons in the electron sample is estimated to be less than 0.01%.

Pion samples are made by removing the electrons and muons from the inclusive-trigger data. Electrons are efficiently removed by requiring that both Cherenkov counters must have signals consistent with pedestals. Most of muons are removed by using the pulse height of the muon counter. The fractions of electrons and of muons in the pion sample are estimated to be less than 0.1% and 1.0%, respectively. In 1 GeV/c beam, however, pion events cannot be discriminated from muon events very well because 1 GeV/c muon does not penetrate the calorimeter. We therefore do not have 1 GeV/c pion data sample.

Pulse-height distributions for 4 GeV/c electrons and pions are shown in Fig. 9. Energy resolution is obtained by a Gaussian fit. The results are summarized in Table 2.

A “no-leak” sample is made as a subset of each full sample described above, to see the effect of longitudinal shower leakage. Events in which the most downstream RCAL superlayer has signal consistent with the pedestal are selected. Responses of full samples and no-leak samples are compared to estimate performance of a sufficiently thick calorimeter module.

3.2 High-energy Beam Test at FNAL (T912)

3.2.1 Setup

The high-energy beam test (T912) was carried out at FNAL meson test beamline (MT6) in September 1999. Unseparated negative charged beams of 10 $\sim$ 200 GeV/c were utilized. The experimental setup is schematically shown in Fig. 10. A pair of single-wire drift chambers (SWDCs) were installed at both upstream and downstream of the momentum analyzing magnet to determine the particle momentum. At the downstream of the momentum analyzing magnet, there was a synchrotron radiation detector (SRD) for electron identification. In front of the calorimeter, three scintillation counters (T4,T5,TPSD), which have a coincidence area of 40 mm $\times$ 40 mm, were installed. The calorimeter module was placed on a stage which can move both horizontally and vertically. RCAL had 10 superlayers in T912. The most downstream superlayer did not have lead absorbers, and was used for muon-tagging and shower-leak veto. At the most downstream of the beamline, a scintillation counter (M1) was installed to identify muons.

An inclusive trigger, a simple coincidence of two trigger scintillation counters T4 and T5, was used for all data taking; all event selections are made offline. Electron and pion data were taken by tuning the beams to be electron-rich and pion-rich, respectively, by choosing proper radiator/absorber combinations. The fraction of muons in a pion-tuned beam was typically 5%. These muons are used for gain calibration. During data taking with the pion-tuned beams, a 50-mm-thick (2.8 X_0) iron block was installed in front of the TPSD counter to reject electrons using its pulse height.

Data were taken for nominal momenta of 10, 25, 50, 75, 100, 150 and 200 GeV/c for pion-tuned beams, and 10, 25, 50, 75, 100 and 150 GeV/c for electron-tuned beams. Calibration data were taken with 50 GeV/c pion-tuned beam injected into the center of each tower. The signals of the calorimeter and other detectors were read out by a PC-based CAMAC system.

3.2.2 Gain Calibration

The gains of FCAL blocks were calibrated using the penetrating muons. Selection criteria of muon events from the data with pion-tuned beam are as follows.

- All of T4, T5, TPSD must have signals consistent with one MIP.
- The signal of any block surrounding the tower to be calibrated should be consistent with the pedestal.
- The most downstream superlayer of RCAL must have a signal consistent with one MIP.

The muon sample used for the calibration of the blocks in the central tower of FCAL is also used to calibrate the RCAL superlayers.

Typical muon pulse-height distributions, shown in Fig. 11, have significant tails. The distributions are fitted with a Landau function, which is expressed as

$$f(x) = A \exp\left(-\frac{y + e^{-y}}{2}\right) \ , \quad y = \frac{x - B}{C} \ .$$

The calibration constant is defined by the parameter B. The stability of the calibration constants against the fitting range variation and the distribution shape deformation caused by photon yield difference of scintillator tiles is examined by a GEANT [5] simulation and found to be within 1% in terms of root of mean squared (RMS). The blocks in the inner nine towers have calibration uncertainties less than 1.5%, while other FCAL blocks are calibrated better than 2.2%. RCAL superlayers are calibrated better than 3.0%.

A relative normalization factor between FCAL and RCAL, α, is determined so that the best energy resolution is obtained for pions:

$$E = E_{\mathrm{FCAL}} + \alpha E_{\mathrm{RCAL}} \quad .$$

The factor α is determined to be 0.71±0.01, which is found to realize a linearity close to the best one.

3.2.3 Beam Momentum Determination

The momentum of incoming particles is measured using two pairs of SWDCs located upstream and downstream of the momentum analyzing magnet. The nominal and measured momenta are summarized in Table 3 together with the measured momentum spread. The dominant source of the measured momentum spread is assumed to be reconstruction resolution, since accelerator experts calculated the beam momentum spread to be only 0.26% [6] for pion-tuned beams (secondary beams). For electron-tuned beams (tertiary beams), however, the beam momentum spread is not calculated.

A correlation plot between the measured momentum and the energy measured by the calorimeter is demonstrated in Fig. 12. As a weak positive correlation can be seen only for electrons, the momentum spread of electron-tuned beams should be significantly larger than that of the pion-tuned beams. We use the measured particle momentum in the following analysis.

3.2.4 Event Selection

In the T912 beam test, the beam contained many multi-particle events caused by interactions of particles with the beamline materials upstream of the calorimeter. In order to reject such events, the following cuts are applied.

- All trigger counters (T4, T5 and TPSD) should have signals consistent with one MIP.
- Each SWDC wire should have one and only one hit, and the two timing signals from two planes in pair are consistent with a passage of a single particle.

After these cuts, particle identification is performed using M1, SRD, and calorimeter signals. Electrons are selected as follows (see Fig. 13).

- The M1 signal should be consistent with the pedestal.
- The particle must deposit more than 98% of the energy in the section 1 of FCAL.

- The SRD signal must be well above the pedestal for nominal momentum of 75 GeV/c or higher.

Pions are selected as follows.

- Sum of the signals over FCAL sections 2, 3, 4 and RCAL must be larger than 0.44 MIP-equivalent (electron rejection).

- Sum of the signals over the whole calorimeter must be more than 2.2 MIP-equivalent (muon rejection).

An example of pion selection using the calorimeter signals is shown in Fig. 14.

Typical energy distributions for electrons and for pions are shown in Fig. 15 for a nominal momentum of 50 GeV/c. As a result of the hardware compensation, the energy distribution for pions is well fitted with a Gaussian function. The obtained energy resolutions are summarized in Table 4.

Similar to T411, no-leak samples are made using the pulse height of the most downstream superlayer of RCAL.

3.3 Systematic Uncertainties

3.3.1 Systematic Uncertainties within each Beam Test

The following effects have been evaluated as sources of systematic uncertainties on the energy resolution in each beam test.

(i) Statistical uncertainty of the calibration constants.
Propagation of the statistical uncertainty of the calibration constants to the energy resolution is estimated by varying the calibration constants according to their statistical uncertainties.

(ii) Gain drift.
The gain of each FCAL block is traced using LED light sources in T411, and using muon events in T912. From the data, the drift is estimated to be 1.9% for T411, and 2.0% for T912, averaged over all blocks. The effect on the energy resolution is calculated to be 0.2% at most by changing calibration constants according to the variation.

(iii) ADC pedestal fluctuation.
Pedestals are continuously monitored through the data taking at off-spill timing. The pedestal fluctuation is estimated to introduce an uncertainty of the calibration constants of about 0.1% for T411. In T912, the effect is negligibly small.

The systematic uncertainties of the energy resolution are summarized in Table 5. The systematic uncertainties of the linearity and e/π ratio are obtained in a similar way and are included in Tables 7 and 8.

In T912 the current of the momentum analyzing magnet was very stable (~0.01%) except for the lowest momentum of 10 GeV/c, where a 4% fluctuation was observed.

3.3.2 Systematic Uncertainties between T411 and T912

The order of the lead plates and the scintillators were totally changed between T411 and T912. This change introduced systematic uncertainties listed below.

(i) Variation of the lead plate thickness.
Lead plates have thickness variation of 1.3%.

(ii) Variation of average photon yield of scintillator tiles.
Distribution of the average photo-electron yield of 2000 tiles used in FCAL and that of RCAL scintillator plates are shown in Fig. 16. These are measured with a β-ray source using a common PMT. The FCAL tiles and the RCAL scintillator plates have 14.6% and 14.3% variation in photo-electron yield, respectively, in terms of RMS.

(iii) Non-uniformity of the response in each FCAL tile and RCAL scintillator.
A response map of photo-electron yield in a FCAL tile is shown in Fig. 17. The four corners have significantly low photon yield, while the area close to the WLS fibers has a slightly high photon yield.

Effects of the above items are evaluated with a GEANT3 simulation with the GHEISHA package. Cut-off energies of 10 keV and 500 keV are used for electromagnetic particles and for hadrons, respectively. The result of the simulation for the item (ii) in the case of 3 GeV/c pion is shown in Fig. 18. Deviation of energy resolution from the sample with no photon-yield variation is plotted for 100 samples with photon-yield variation, where photon-yield of tiles are varied according to the variation shown in Fig. 16. It is seen that this variation has only 0.56%-effect on the energy resolution. Effect of the item (iii) is also estimated in a similar way to the item (ii). The other major systematic uncertainty, variation of the lead-thickness, has nearly the same effect as discussed elsewhere [2], which is about 0.4% typically. The inter-connection uncertainties are equally assigned to both T411 and T912 data for overall fitting of the energy resolution. All systematic uncertainties of σ_E/E for combination of T411 and T912 are summarized in Table 6.

4 Results

4.1 Energy Resolution

Energy resolutions obtained from T411 and T912 are plotted in Fig. 19. Energy resolution is expressed by the following parameterization:

$$\sigma_E/E = \sigma_{stochastic}/\sqrt{E} \oplus \sigma_{constant} \ .$$

In general, $\sigma_{stochastic}$ and $\sigma_{constant}$ are called stochastic term and constant term of the energy resolution, respectively. The sources of the constant term are considered to be calibration uncertainty, shower leakage and non-uniformity of the calorimeter. On the other hand, sampling fluctuation, statistical fluctuation of the number of photoelectrons, fluctuation of the number of shower particles contribute to the stochastic term.
The results of fittings are

$$\frac{\sigma_E}{E} = \frac{(46.7 \pm 0.6)\%}{\sqrt{E}} \oplus (0.9 \pm 0.9)\% \quad \text{for pions, and}$$

$$\frac{\sigma_E}{E} = \frac{(23.9 \pm 0.3)\%}{\sqrt{E}} \oplus (0.8 \pm 0.3)\% \quad \text{for electrons.}$$

Energy resolutions for no-leak samples are shown in Fig. 20. The same fitting procedure results in a pion energy resolution of

$$\frac{\sigma_E}{E} = \frac{(46.5 \pm 0.6)\%}{\sqrt{E}} \oplus (0.0^{+0.5}_{-0.0})\% \ .$$

The pion energy resolution is not as good as the design value which was achieved at the low energy beam tests [2] with no acryl plates. Present result of the tile/fiber module is consistent with the result of the straight-groove module with acryl plates given in Table 1. We can thus conclude that deterioration of the stochastic term is caused by the acryl plates. The "no-leak" sample analysis shows that longitudinal shower leakage is not the cause of deterioration the stochastic term.

4.2 Linearity

The measured energies and the deviations from a linear function are shown in Fig. 21. A relative normalization factor to connect T411 and T912 measurements is determined by 4 GeV/c electron data and 49.1 GeV/c electron data. Except for the 200 GeV/c data, deviations are at a level of $\pm 1\%$, while 200 GeV/c data have a significant deviation of 2%. It is unlikely that this originates from gain saturation of PMTs since the deviation is observed not only for electrons but also for pions with nearly the same amount. Saturation of the momentum analyzing magnet current could have caused this effect. Deviations from linearity are summarized in Table 7.

4.3 e/π Ratio

The ratios of measured energies for electrons to those for pions (e/π ratios) are plotted in Fig. 22. Unfortunately, the beam momentum for pions are different from those for electrons. Since the response of calorimeters to electromagnetic showers generally has a better linearity than that to hadronic showers, the electron response is scaled to the pion beam momentum and the e/π ratio is calculated.

At low energies, the average of the e/π ratios is 1.042 ± 0.010. For 4 GeV/c data, the e/π ratio is measured to be 1.026 ± 0.018, which is consistent with the results of the straight-groove module both without acryl plates and with acryl plates located downstream-side of scintillator plates. Therefore we conclude that acryl plates in the tile/fiber module do not affect the e/π ratio with present configuration, and hardware compensation is retained.

At high energies, average of the e/π ratio is 0.987 ± 0.007, approaching to 1. This behavior is understood by the hadronic shower mechanism in which more fraction of energy is transfered to π^0 production at higher energy. The e/π ratios are summarized in Table 8.

5 Conclusions

We have constructed a compensating tile/fiber hadron calorimeter, and measured the energy resolution, the linearity and the e/π ratio in the energy range from 1 to 200 GeV.

The energy resolution for pions is measured to be $\sigma_E/E = (46.7 \pm 0.6)\%/\sqrt{E} \oplus (0.9 \pm 0.9)\%$ for full samples, and $\sigma_E/E = (46.5 \pm 0.6)\%/\sqrt{E} \oplus (0.0^{+0.5}_{-0.0})\%$ for no-leak samples.

A good linearity is obtained for the energy range from 2 to 150 GeV with deviations about $\pm 1\%$.

In both low- and high-energy regions, the e/π ratios are close to 1.

6 Acknowledgements

We wish to thank the accelerator staffs of High Energy Accelerator Research Organization and Fermi National Accelerator Laboratory. This work was supported in part by a Grand-in-Aid for Scientific Research from Ministry of Education, Science and Culture under contract No. 10554008, an R&D promotion program of High Energy Accelerator Research Organization, and Japan-U.S. Cooperative Research Program in High Energy Physics. JPD and TK were supported in part by DOE grant No. DE-FG03-95ER40917.

References

[1] JLC-I, JLC Group, KEK Report, **92-16**, 1992.

[2] T. Suzuki *et al.*, Nucl. Instr. and Meth. **A 432** (1999) 48.

[3] E. Bernandi *et al.*, Nucl. Instr. and Meth. **A 262** (1987) 229.

[4] K. Hara *et al.*, Nucl. Instr. and Meth. **A 348** (1994) 139.

[5] R. Brun *et al.*, GEANT3, CERN DD/EE/84-1, 1987.

[6] C. N. Brown, T. R. Kobilarcik, FERMILAB-TM-2108, May 2000.

[7] K. Kawagoe *et al.*, Nucl. Instr. and Meth. **A**, submitted for publication

[8] The CDF II Collaboration, The CDF II Detector Technical Design Report, FERMILAB-Pub-96/390-E, 1996.

[9] T. Asakawa *et al.*, Nucl. Instr. and Meth. **A 340** (1994) 458.

[10] S. Aota *et al.*, Nucl. Instr. and Meth. **A 352** (1995) 557.

[11] S. Aota *et al.*, Nucl. Instr. and Meth. **A 357** (1995) 71.

[12] S. Kim (CDF Collaboration), Nucl. Instr. and Meth. **A 360** (1995) 206.

Table 1
Energy resolutions and e/π ratios with and without acryl plates for 4 GeV/c electrons and pions.

	σ_E/E for electrons	σ_E/E for pions	e/π ratio
No acryl plates	(12.0±0.5)%	(20.5±0.4)%	1.03±0.02
Acryl plates upstream	(11.6±0.5)%	(22.7±0.4)%	1.07±0.02
Acryl plates downstream	(12.0±0.5)%	(22.8±0.4)%	1.01±0.02

Table 2
Energy resolutions at the low-energy beam test (T411) at KEK.

Injected particle	Beam momentum (GeV/c)	σ_E/E (%)	Statistical uncertainty (%)	Systematic uncertainty (%)
pion	2	32.7	±0.4	±0.3
	3	27.5	±0.3	±0.3
	4	23.8	±0.3	±0.2
electron	1	23.2	±0.3	±0.2
	2	17.0	±0.2	±0.1
	3	13.4	±0.1	±0.1
	4	12.0	±0.1	±0.1

Table 3
Nominal and measured momenta, measured momentum spread, and normalization uncertainty of momentum in T912.

Injected particle	Nominal momentum (GeV/c)	Measured momentum (GeV/c)	Measured momentum spread (RMS) (%)	Normalization uncertainty of momentum centroid (%)
pion	10	9.5	1.4	4.0
	25	24.0	0.9	1.5
	50	49.1	0.9	0.8
	75	73.4	0.8	0.1
	100	96.6	0.8	$\leq$0.1
	150	146.6	0.9	0.1
	200	200.8	0.7	0.3
electron	10	9.2	1.4	2.3
	25	27.8	1.6	1.2
	50	55.5	1.5	0.1
	75	83.2	1.6	0.1
	100	101.2	1.4	0.3
	150	187.7	1.3	0.4

Table 4
Energy resolutions at the high-energy beam test (T912) at FNAL.

Injected particle	Beam momentum (GeV/c)	σ_E/E (%)	Statistical uncertainty (%)	Systematic uncertainty (%)
pion	9.5	14.2	±0.4	±0.2
	24.0	9.3	±0.1	±0.1
	49.1	6.5	±0.1	±0.1
	73.4	5.5	±0.1	±0.1
	96.6	4.8	±0.1	±0.1
	146.6	4.0	±0.1	±0.1
	200.8	3.6	±0.1	±0.1
electron	9.2	9.4	±0.3	±0.1
	27.8	4.9	±0.1	±0.1
	55.5	3.3	±0.1	±0.1
	83.2	2.8	±0.1	±0.1
	101.2	2.5	±0.1	±0.1
	187.7	1.9	±0.1	±0.1

Table 5
Systematic uncertainties of energy resolution ($\Delta(\sigma_E/E)$).

Injected particle	Beam momentum (GeV/c)	Statistical uncertainty of calibration (%)	PMT gain fluctuation (%)	ADC pedestal fluctuation (%)
pion	2.0	0.1	0.2	0.2
	3.0	0.1	0.2	0.1
	4.0	0.1	0.2	0.1
	9.5	0.1	0.2	$\leq$0.1
	24.0	$\leq$0.1	0.1	$\leq$0.1
	49.1	$\leq$0.1	0.1	$\leq$0.1
	73.4	$\leq$0.1	0.1	$\leq$0.1
	96.6	$\leq$0.1	0.1	$\leq$0.1
	146.6	$\leq$0.1	0.1	$\leq$0.1
	200.8	0.1	0.1	$\leq$0.1
electron	1.0	$\leq$0.1	$\leq$0.1	0.2
	2.0	$\leq$0.1	0.1	0.1
	3.0	$\leq$0.1	$\leq$0.1	$\leq$0.1
	4.0	$\leq$0.1	$\leq$0.1	$\leq$0.1
	9.2	$\leq$0.1	0.1	$\leq$0.1
	27.8	$\leq$0.1	$\leq$0.1	$\leq$0.1
	55.5	$\leq$0.1	$\leq$0.1	$\leq$0.1
	83.2	$\leq$0.1	$\leq$0.1	$\leq$0.1
	101.2	$\leq$0.1	$\leq$0.1	$\leq$0.1
	187.7	$\leq$0.1	$\leq$0.1	$\leq$0.1

Table 6
Systematic uncertainties of energy resolution ($\Delta(\sigma_E/E)$) due to the configuration change between T411 and T912.

Injected particle	Beam momentum (GeV/c)	Variation of lead plate thickness (%)	Variation of scintillator photon yield (%)	Scintillator non-uniformity (%)
pion	2.0	0.6	0.5	0.3
	3.0	0.5	0.4	0.3
	4.0	0.4	0.6	0.1
	9.5	0.6	0.6	0.1
	24.0	0.3	0.4	0.2
	49.1	0.4	0.2	1.0
	73.4	0.3	0.3	0.1
	96.6	0.4	0.2	0.5
	146.6	0.2	0.2	0.1
	200.8	0.3	0.2	0.4
electron	1.0	0.5	0.7	0.1
	2.0	0.4	0.4	0.3
	3.0	0.3	0.3	0.7
	4.0	0.3	0.2	0.1
	9.2	0.4	0.4	$\leq$0.1
	27.8	0.2	0.2	0.2
	55.5	0.1	0.2	0.1
	83.2	0.1	0.1	0.1
	101.2	0.1	0.1	0.3
	187.7	0.1	0.1	$\leq$0.1

Table 7
Linearity of the calorimeter.

Injected particle	Beam momentum (GeV/c)	Deviation from linearity (%)	Overall uncertainty of deviation (%)
pion	2.0	−1.6	0.8
	3.0	−1.1	0.4
	4.0	−1.1	0.7
	9.5	3.6	4.0
	24.0	0.9	1.6
	49.1	0.2	0.8
	73.4	0.3	0.1
	96.6	0.9	0.1
	146.6	1.2	0.1
	200.8	−2.0	0.4
electron	1.0	−2.1	0.3
	2.0	0.4	0.3
	3.0	1.1	0.2
	4.0	0.6	0.2
	9.2	2.5	2.4
	27.8	−0.2	1.2
	55.5	0.6	0.1
	83.2	1.3	0.2
	101.2	0.4	0.3
	187.7	−2.0	0.4

Table 8
The e/π ratio of the calorimeter.

Beam momentum (GeV/c)	e/π ratio	Statistical uncertainty	Systematic uncertainty
2.0	1.057	0.005	0.015
3.0	1.041	0.004	0.016
4.0	1.026	0.004	0.017
9.5	0.985	0.005	0.049
24.0	0.978	0.001	0.024
49.1	0.991	0.001	0.017
73.4	0.996	0.001	0.015
96.6	0.980	0.001	0.015
200.8	0.984	0.001	0.016

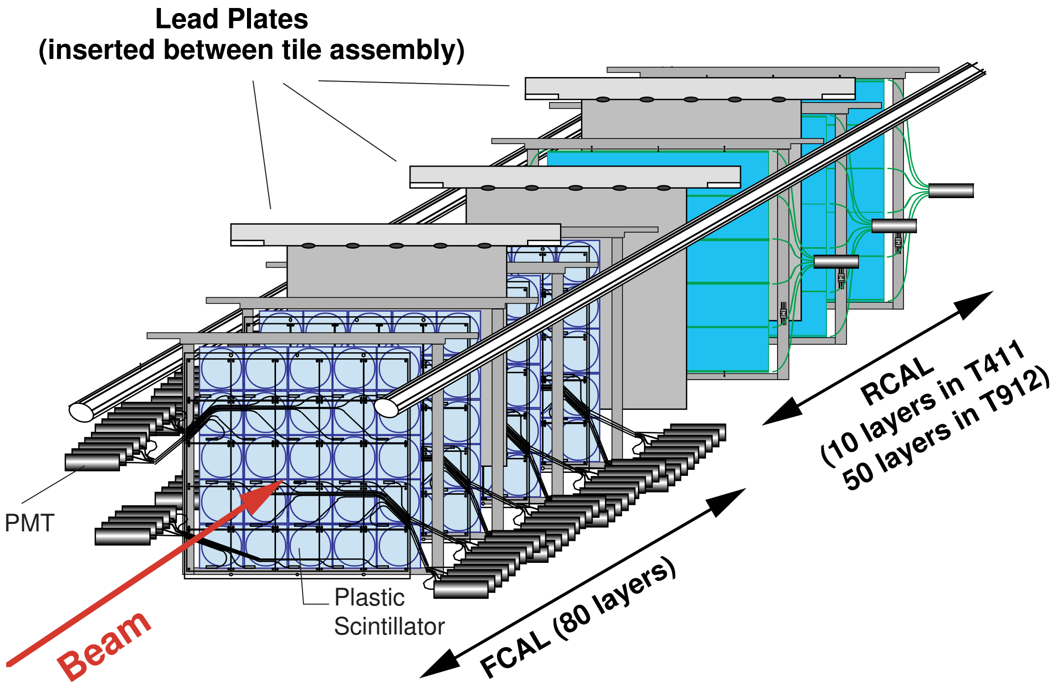

Fig. 1. A schematic view of the calorimeter module.

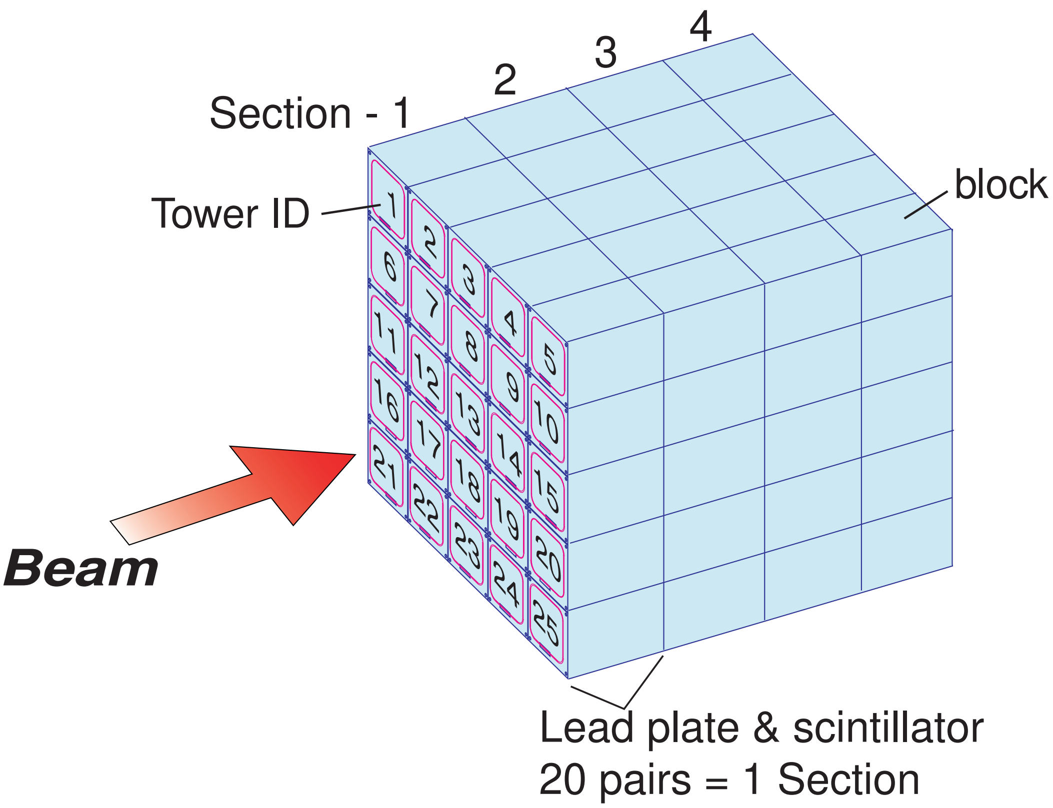

Fig. 2. Segmentation scheme of the front part of the calorimeter (FCAL).

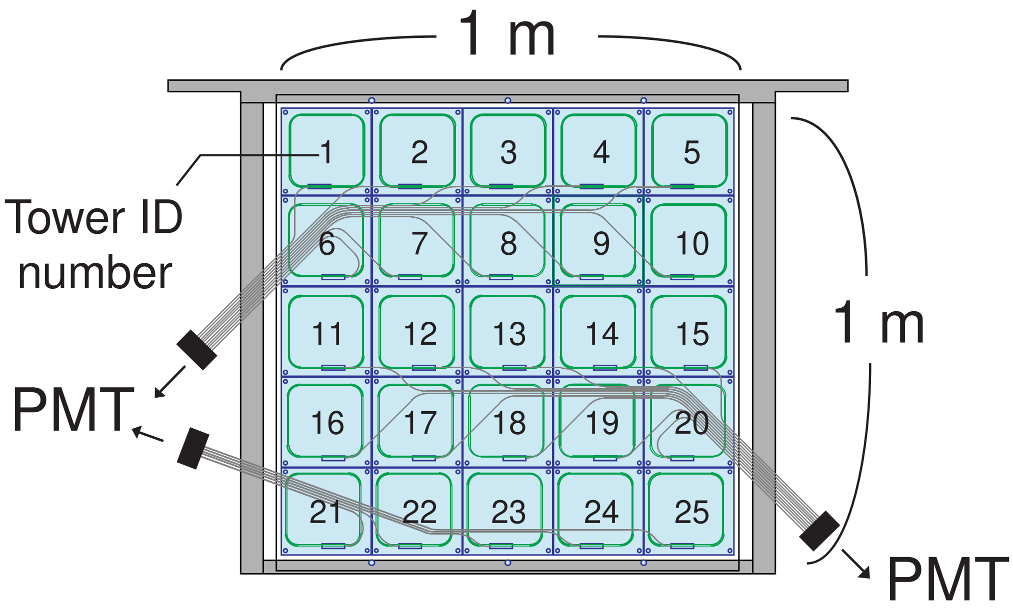

Fig. 3. The optical readout scheme of the tile scintillator assembly used in FCAL.

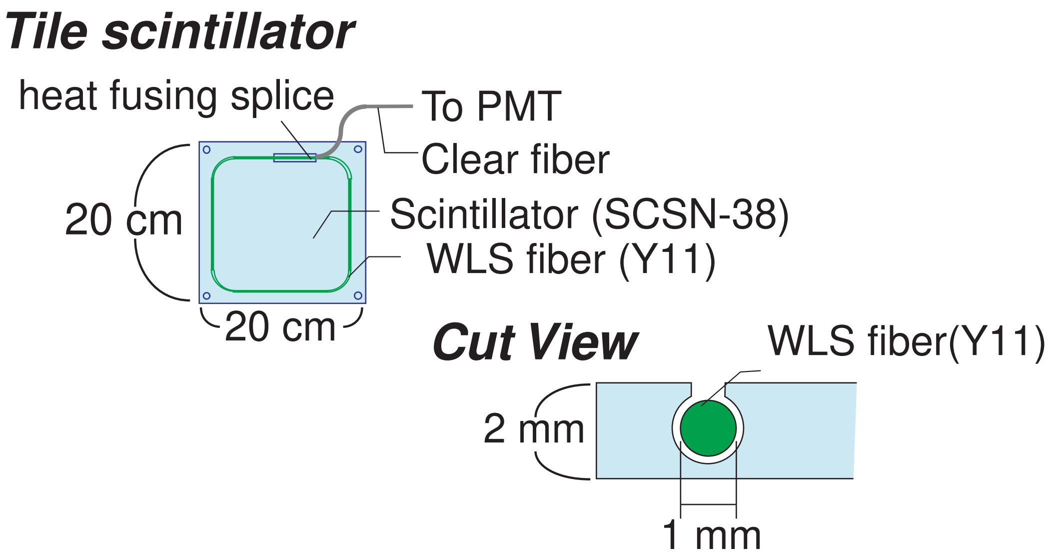

Fig. 4. A schematic view of a scintillator tile and WLS/clear fibers.

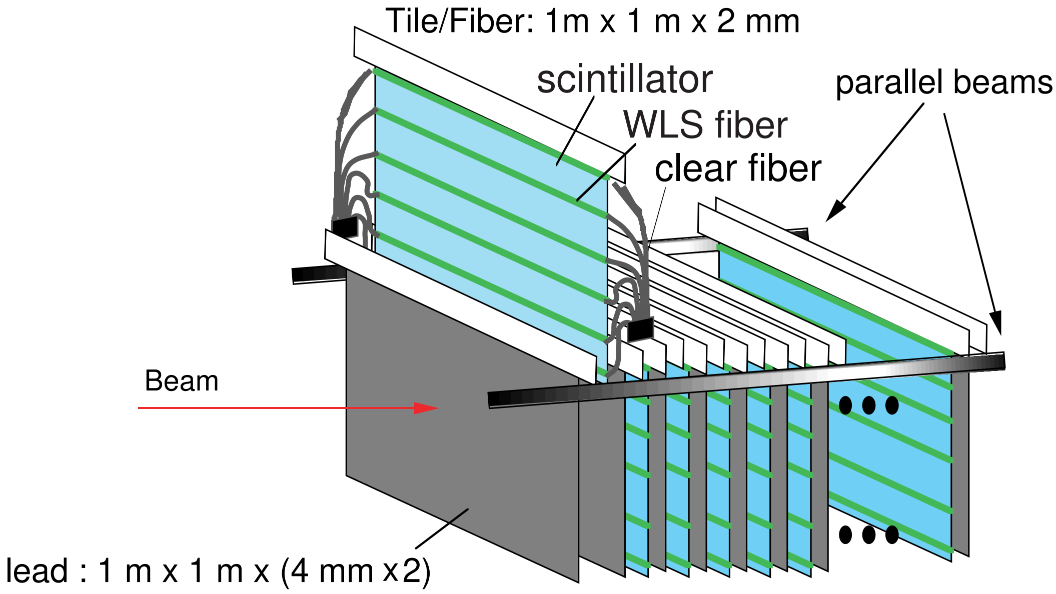

Fig. 5. Configuration of the rear part of the calorimeter (RCAL).

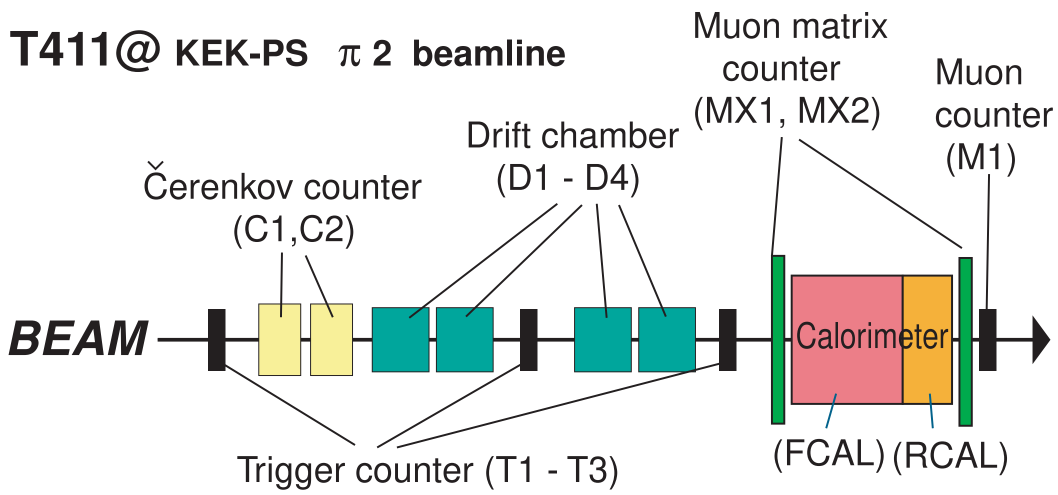

Fig. 6. Layout of the T411 setup.

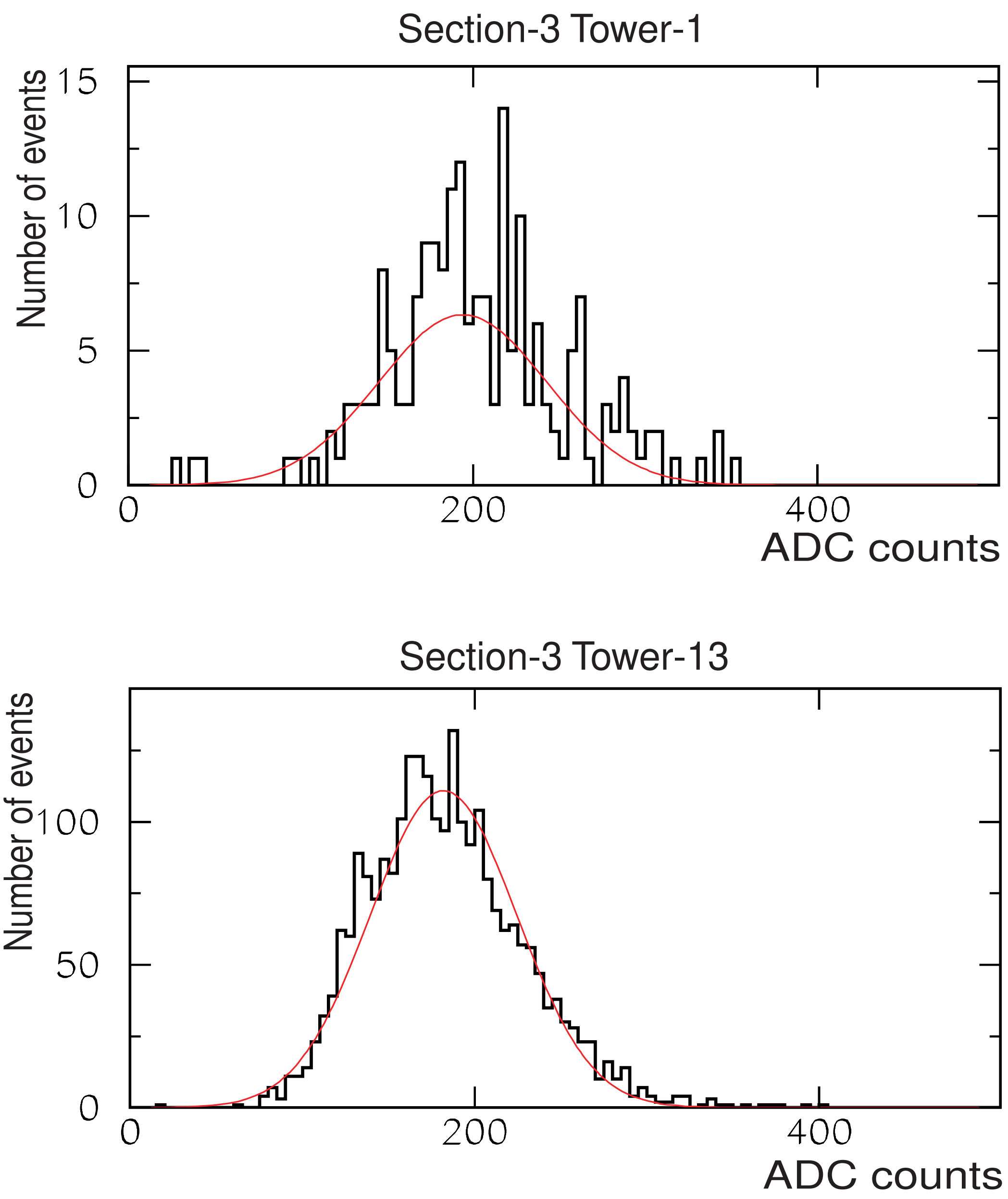

Fig. 7. Typical pulse-height distributions of muons in T411; for the tower 1 at the corner (top), and for the tower 13 at the center (bottom) of the same section.

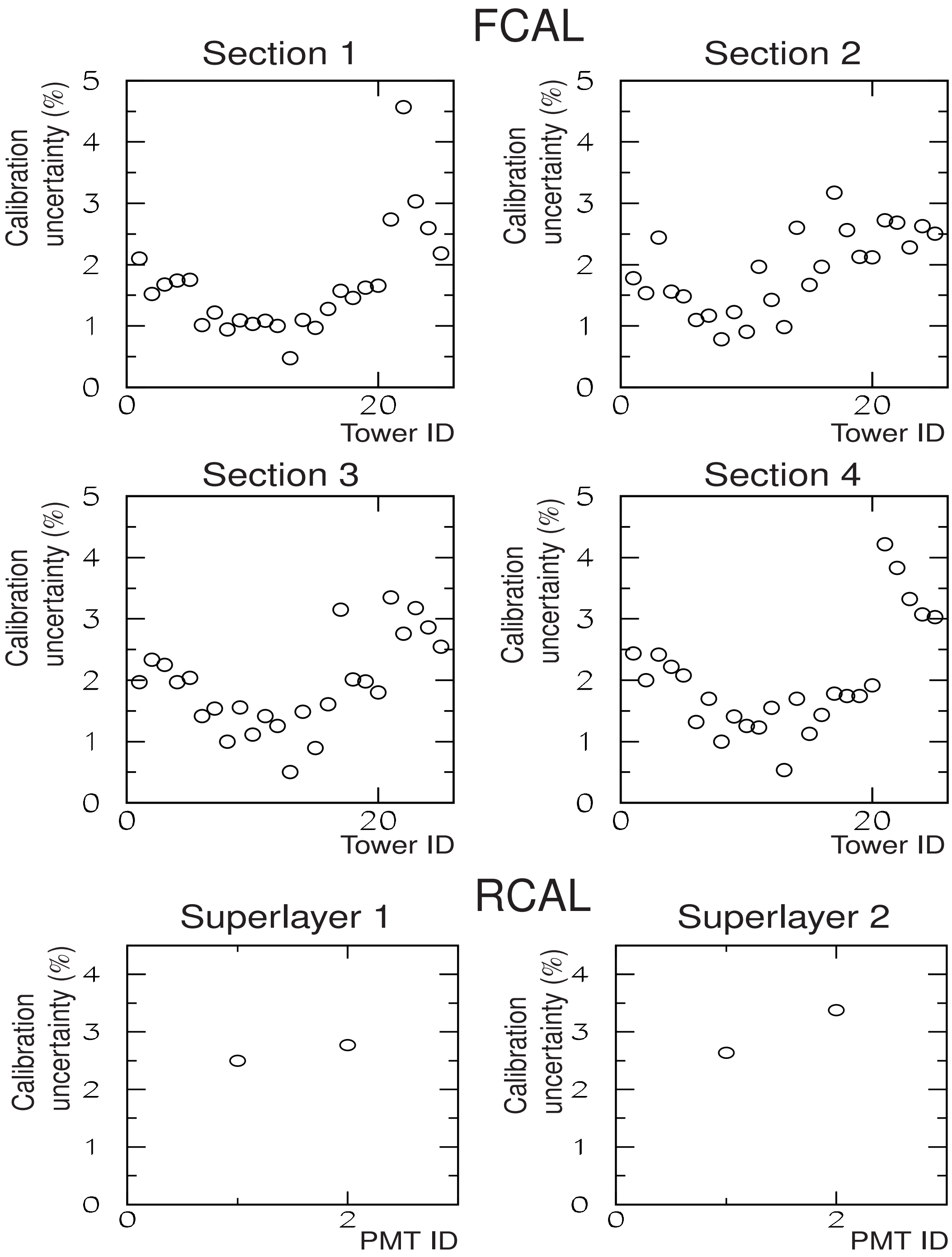

Fig. 8. Statistical uncertainties of the calibration constants in T411.

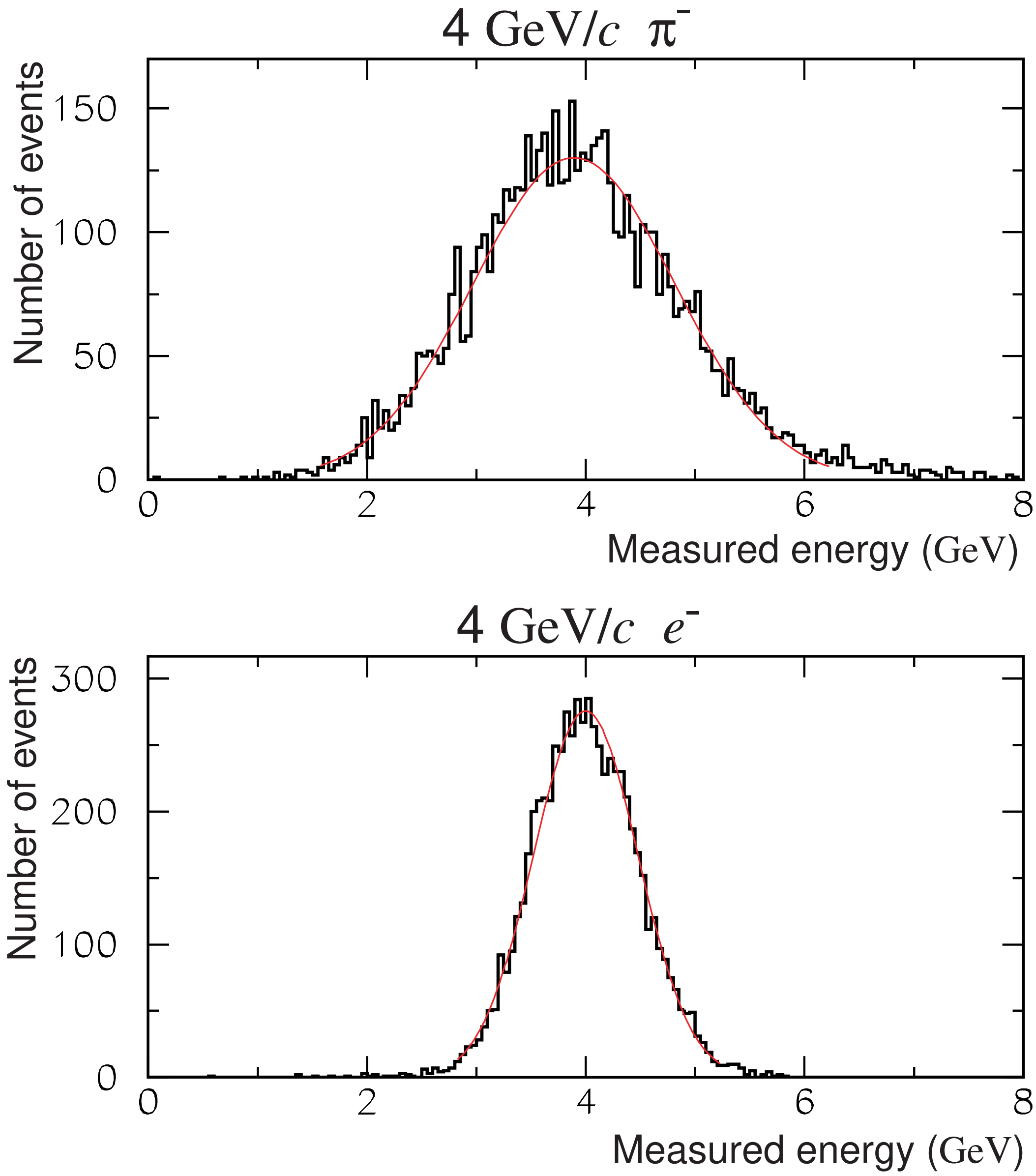

Fig. 9. Measured energy distributions for pions (top) and for electrons (bottom) in T411.

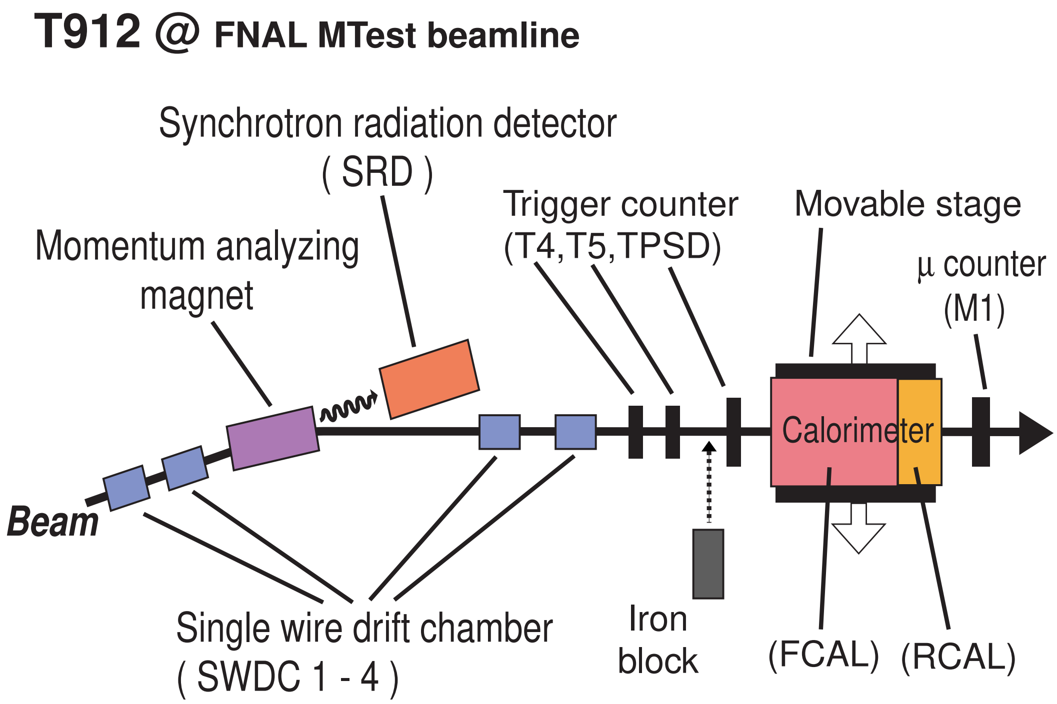

Fig. 10. A schematic view of the T912 beamline setup.

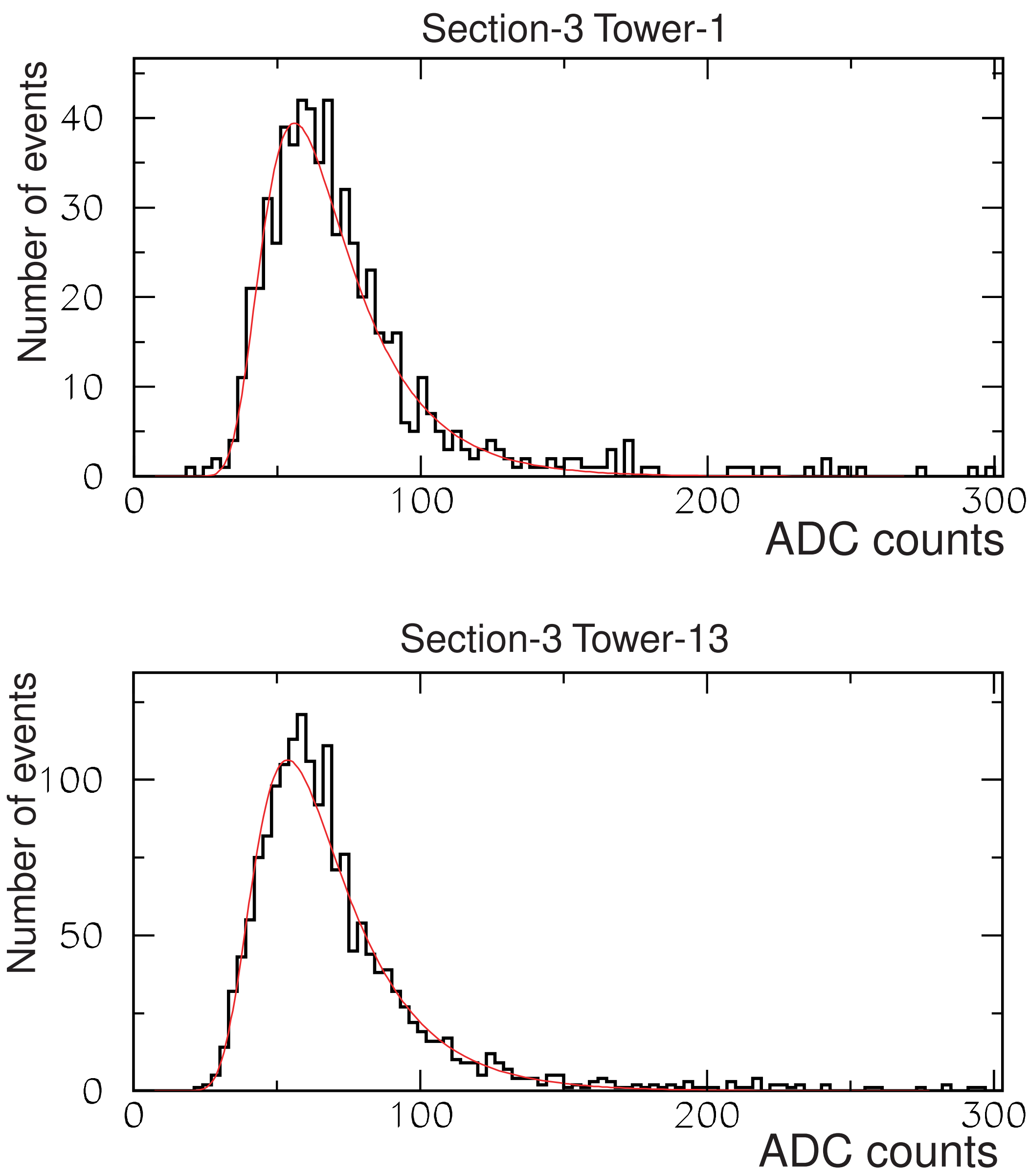

Fig. 11. Typical pulse-height distributions of muons in T912; for the tower 1 at the corner (top), and for the tower 13 at the center (bottom) of the same tower.

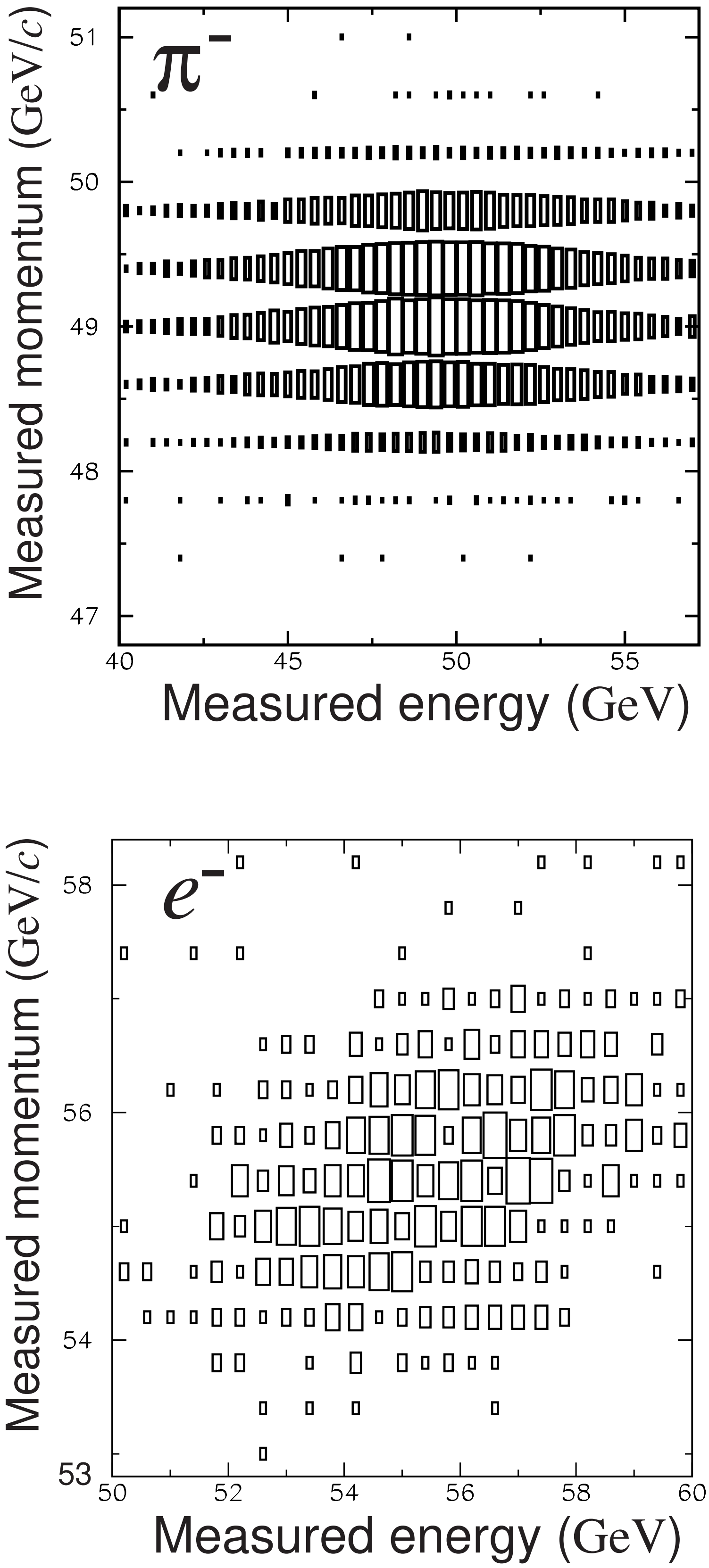

Fig. 12. Correlation between reconstructed particle momentum and measured calorimeter energy; for pions (top), and for electrons (bottom).

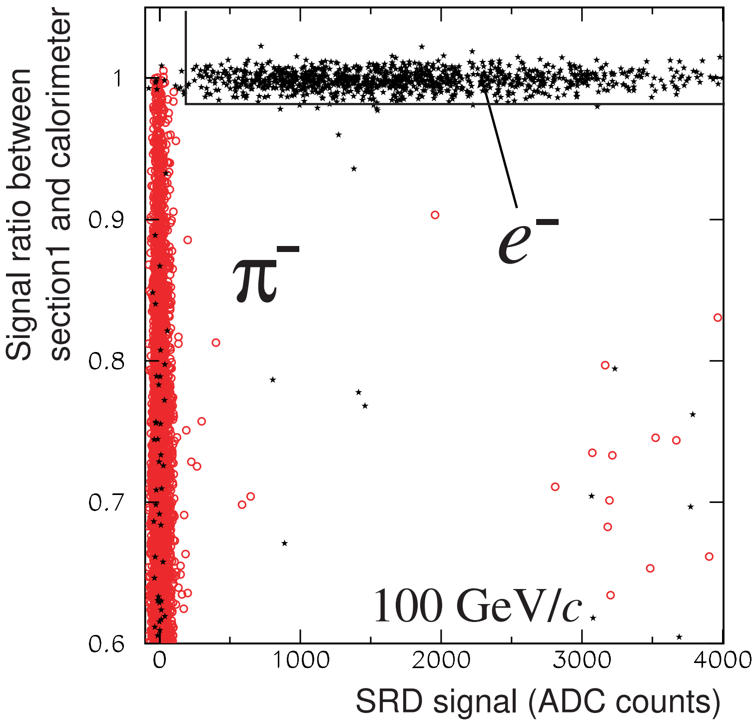

Fig. 13. An example of electron selection using the SRD and the calorimeter signals for the data of nominal momentum 100 GeV/c. Open circle denotes an event in the pion-tuned beams, while star denotes an event in the electron-tuned beams.

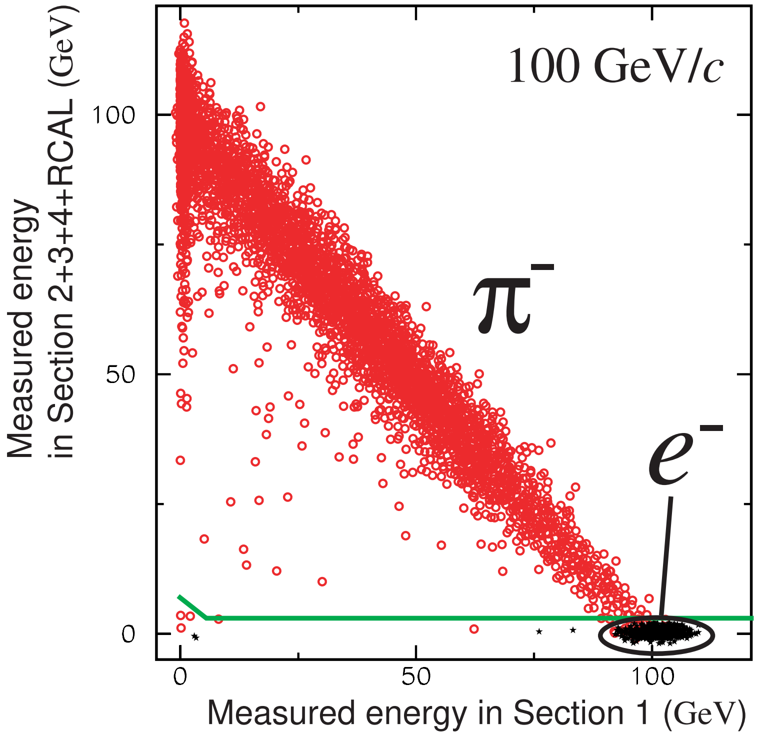

Fig. 14. An example of pion selection using the calorimeter signals for the data of nominal momentum 100 GeV/c. Horizontal axis is energy deposit in section 1, and vertical axis is sum of energy deposit in other sections and RCAL superlayers. Open circle denotes an event in the pion-tuned beams, while star denotes an event in the electron-tuned beams.

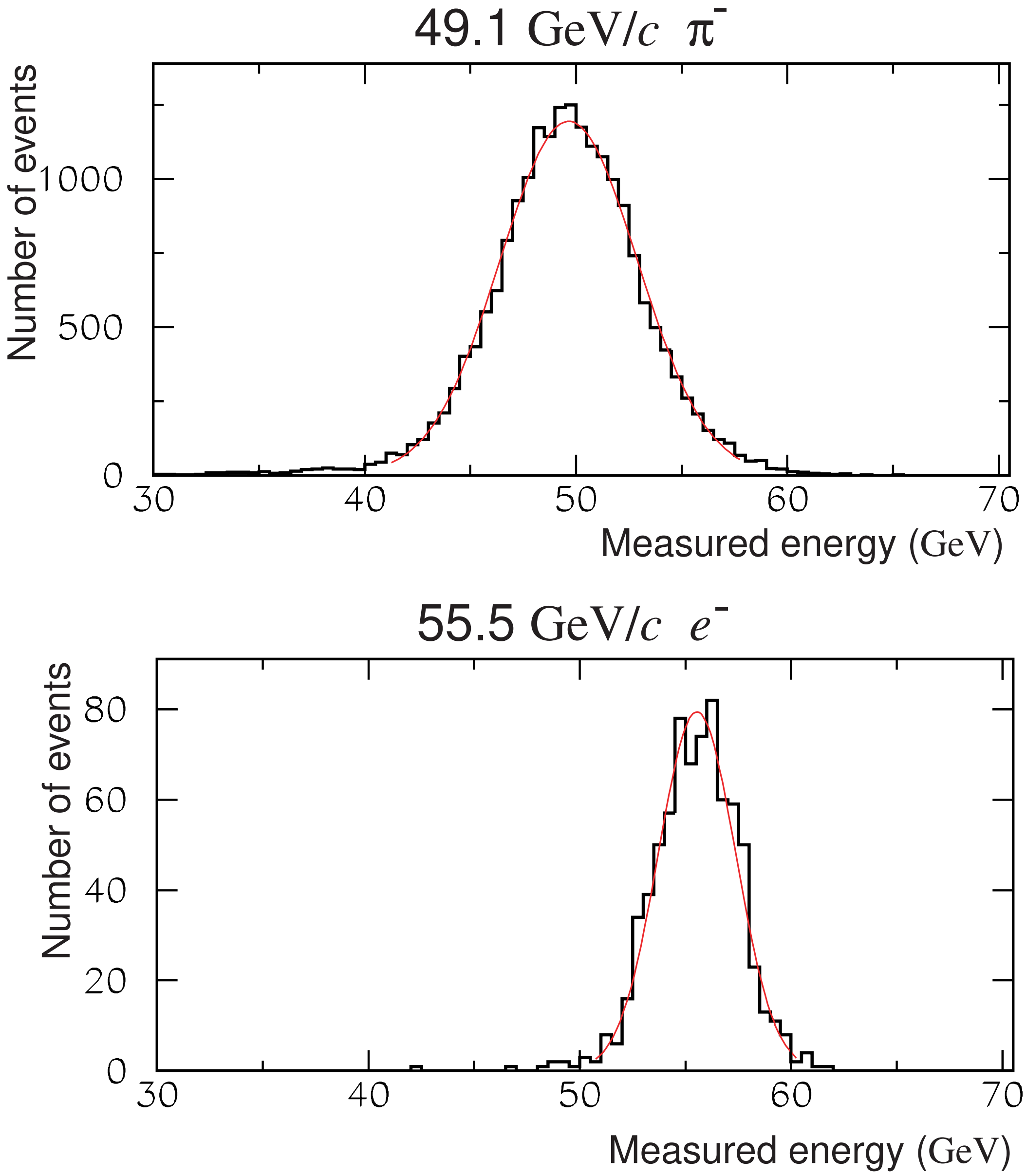

Fig. 15. Typical energy distributions for pions (top) and for electrons (bottom) in T912.

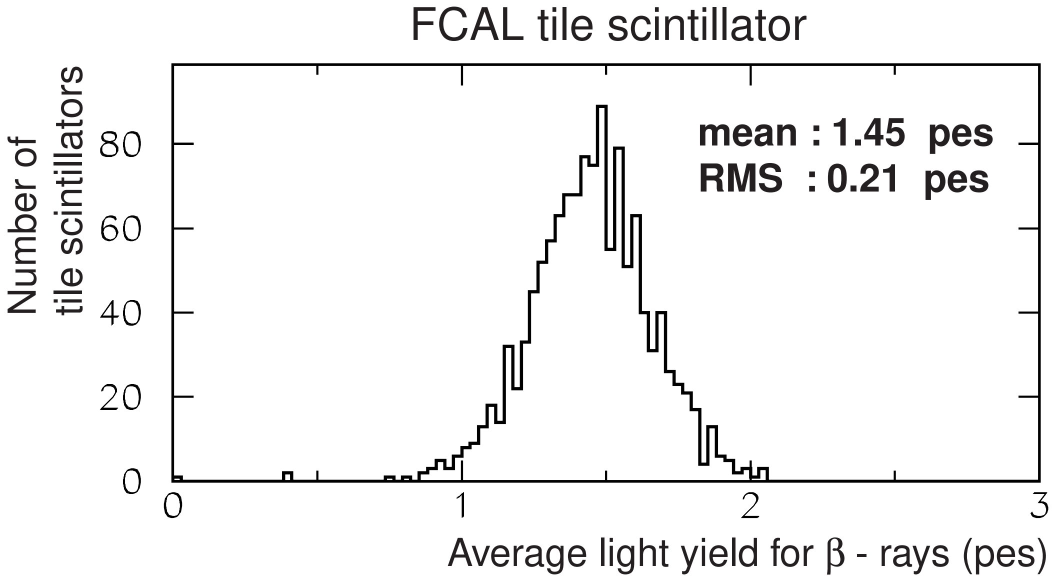

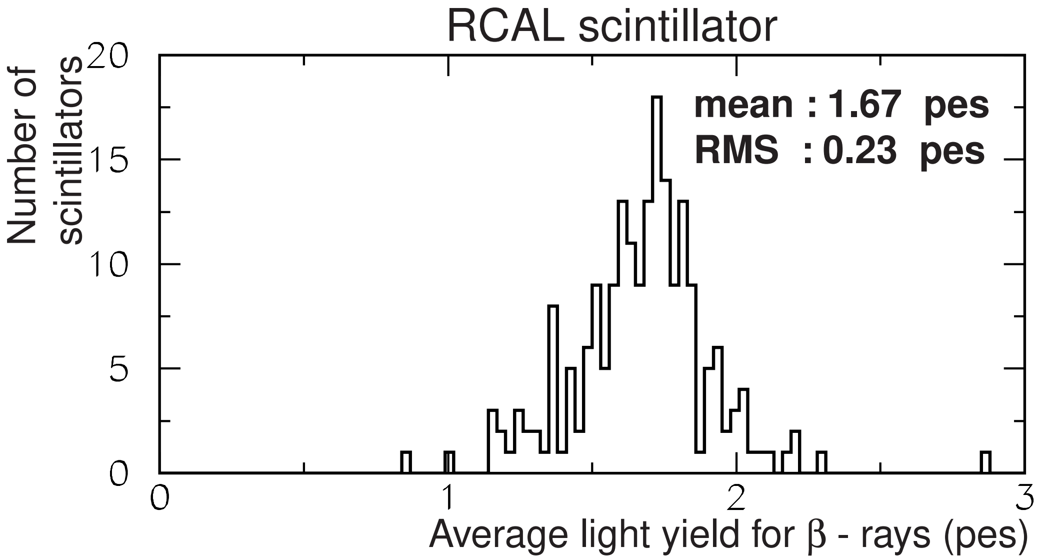

Fig. 16. Photo-electron yields of FCAL scintillator tiles (top) and RCAL scintillator plates (bottom) measured with β-rays. The yields are given in photoelectrons (pes).

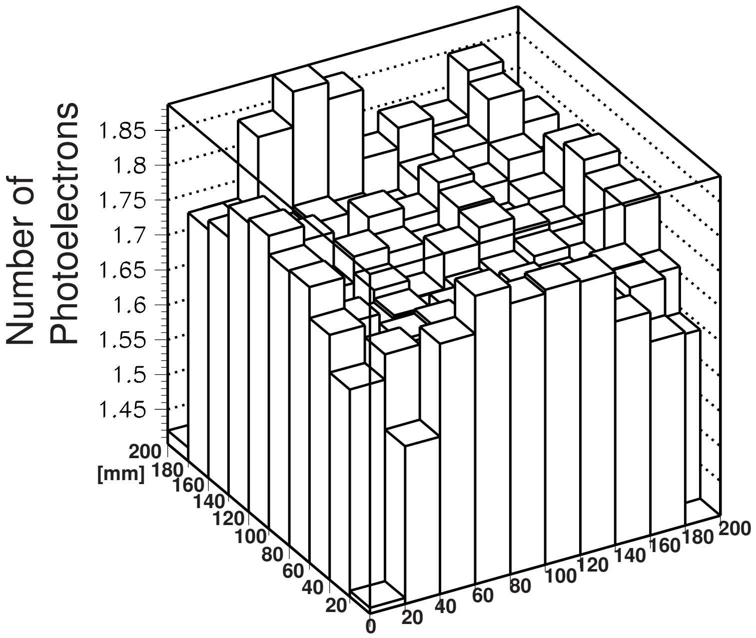

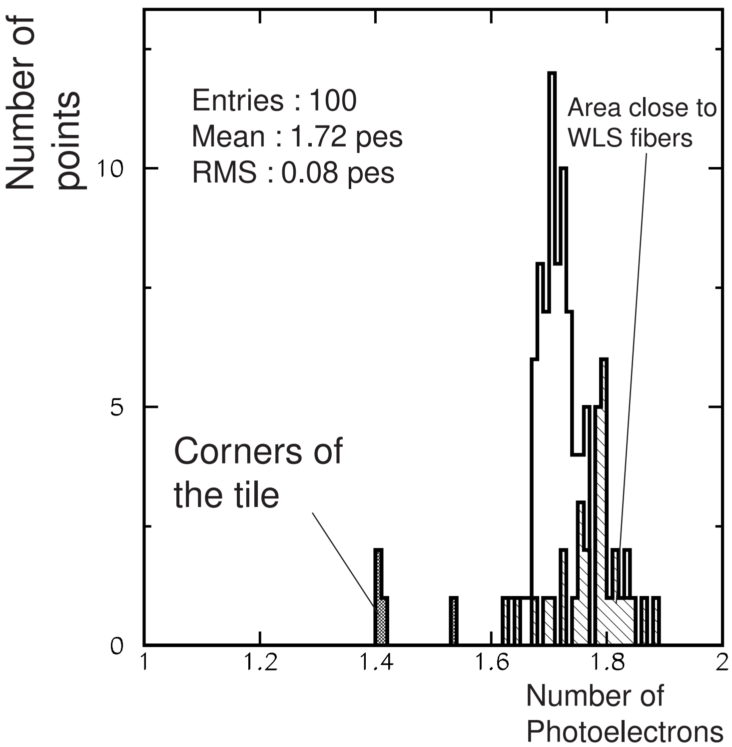

Fig. 17. Uniformity of photo-electron yield over one scintillator tile. A map over a tile (top) and its distribution (bottom).

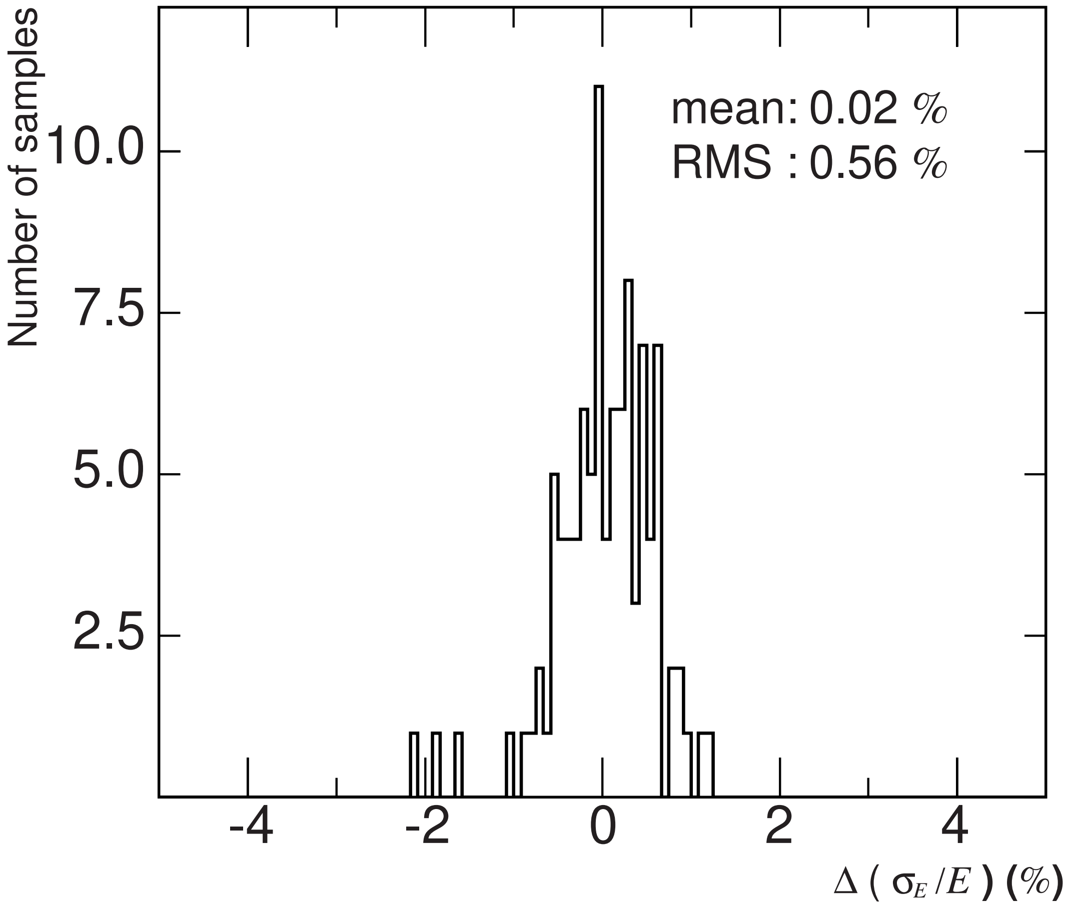

Fig. 18. Deviation of energy resolutions of 100 simulated samples taking account of the variation of photo-electron yield of scintillator tiles from that of a sample without photo-electron yield variation.

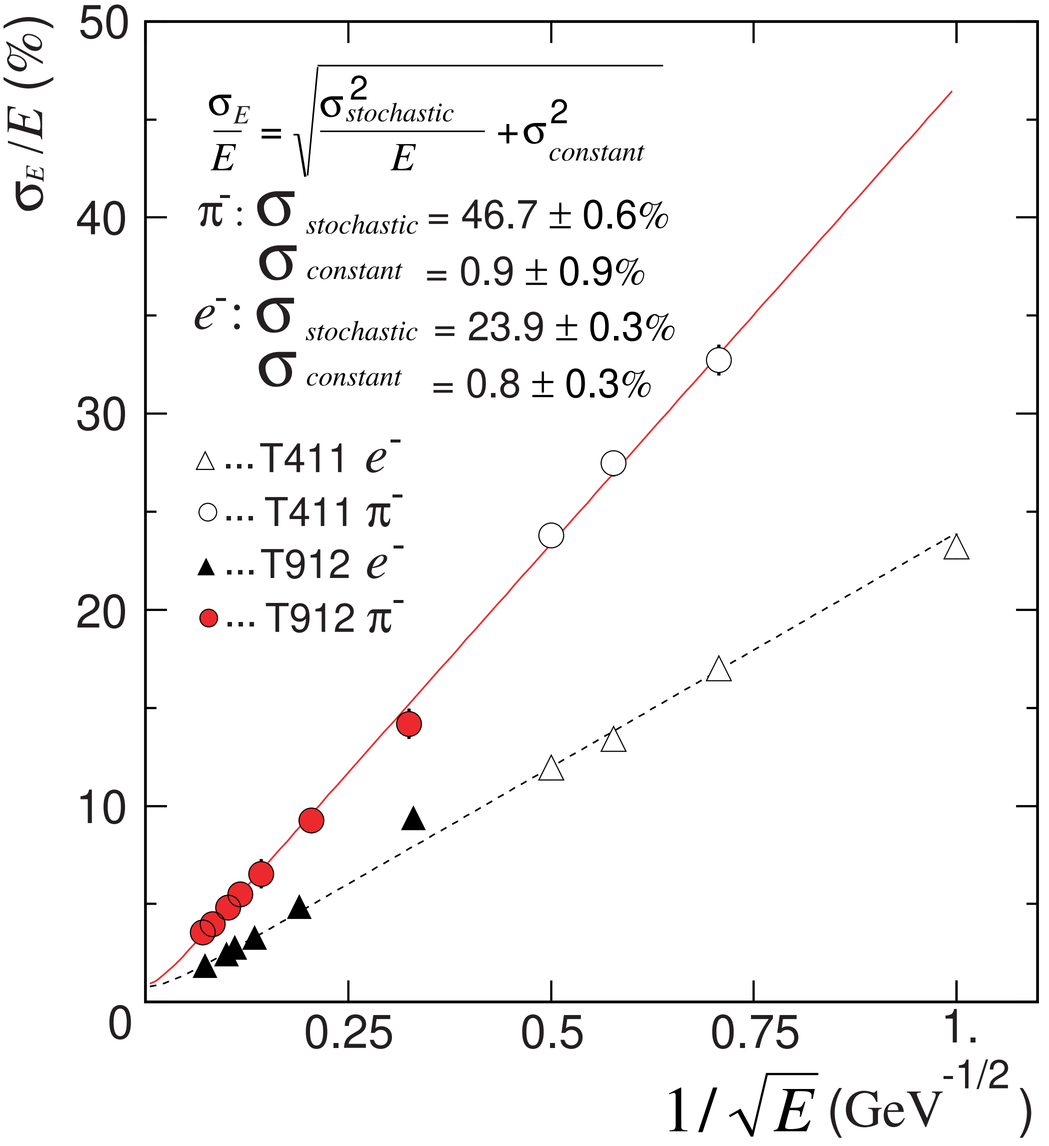

Fig. 19. Energy resolutions of the calorimeter without the shower leakage cut (full sample). The horizontal axis is given by $1/\sqrt{E}$ for ease of interpretation.

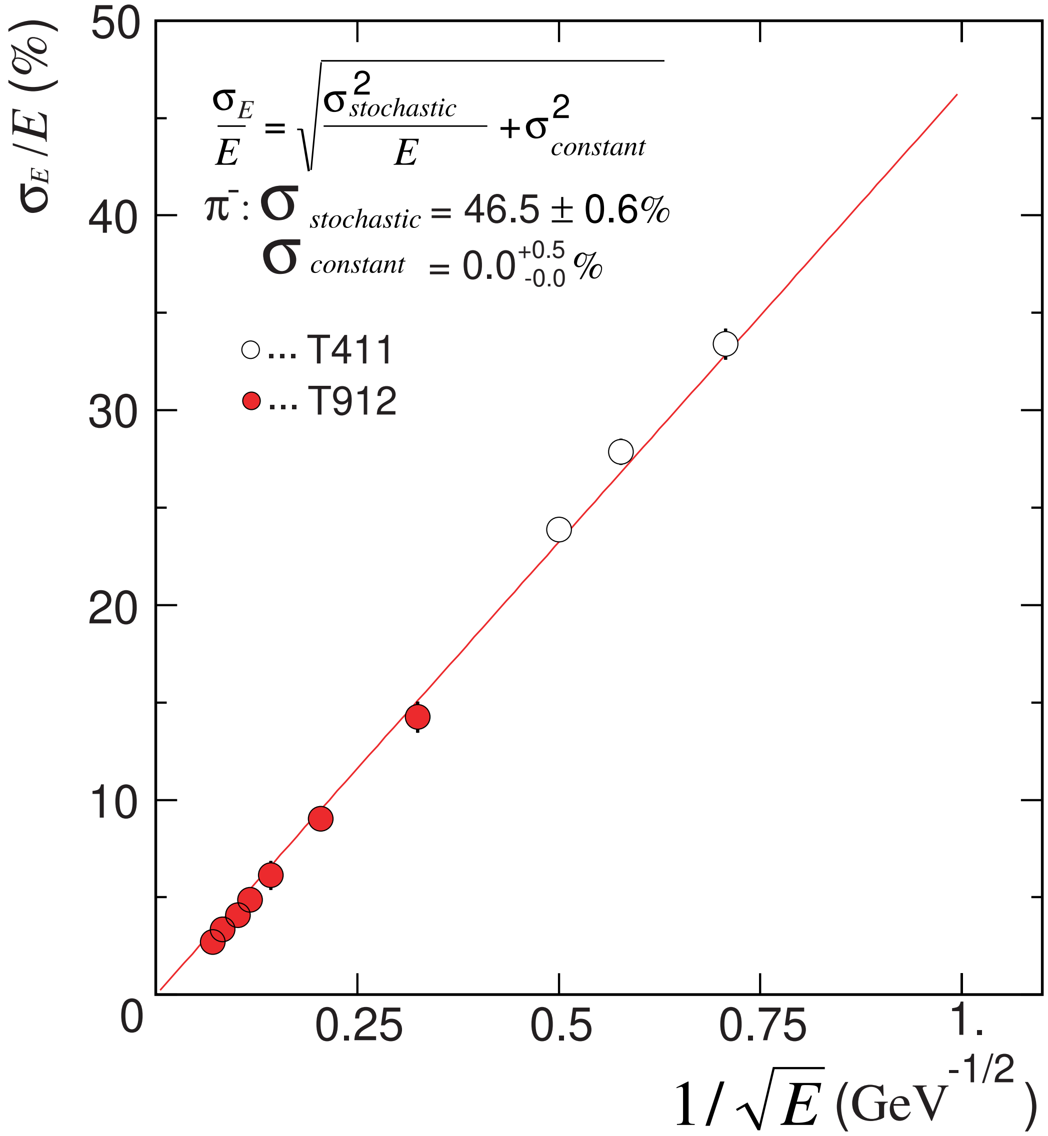

Fig. 20. Energy resolutions of the calorimeter with the shower leakage cut (no-leak sample). The horizontal axis is given by $1/\sqrt{E}$ for ease of interpretation.

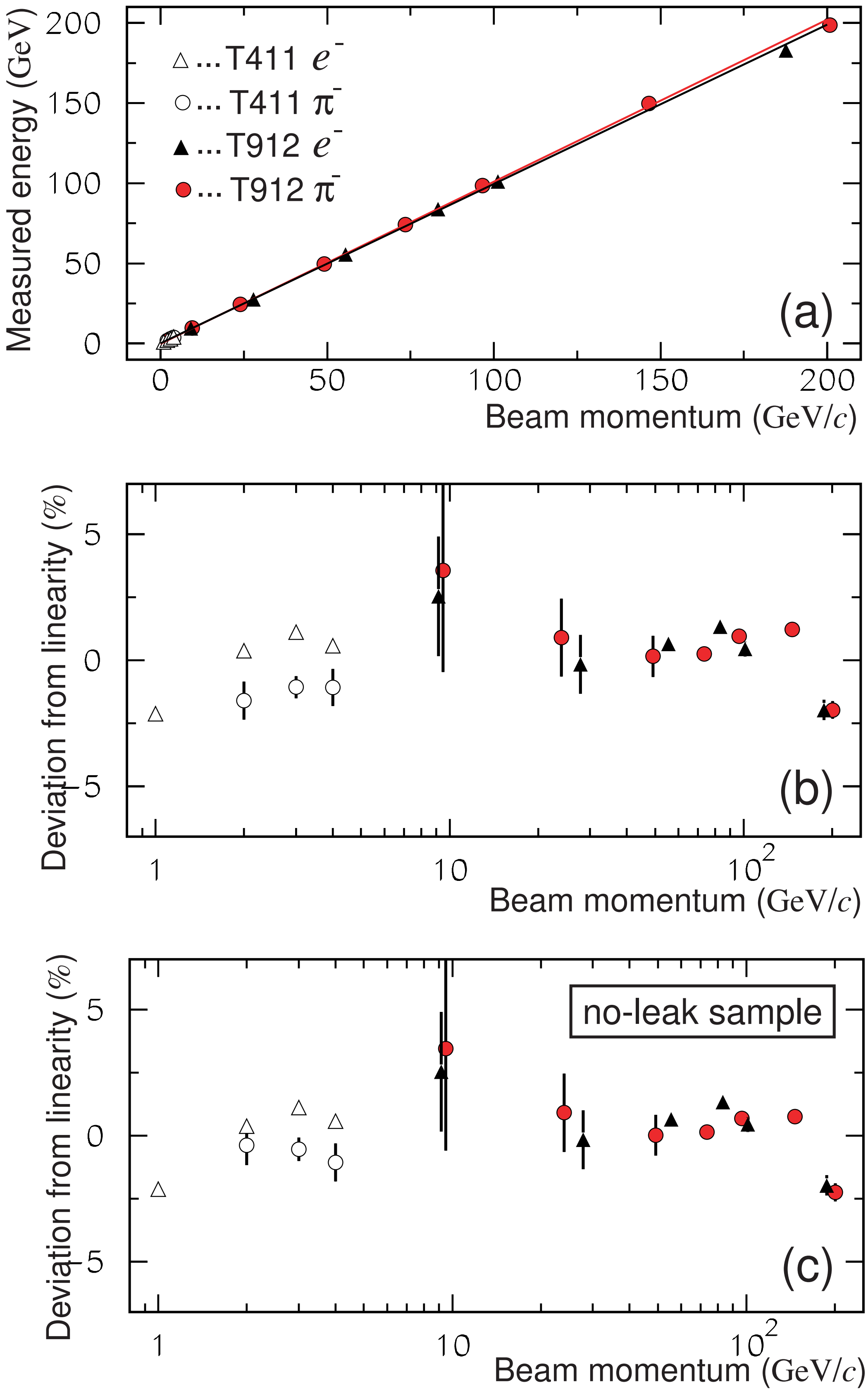

Fig. 21. Linearity of the energy measurement and deviations from a linear function. The plots (a) and (b) are for full samples, while the plot (c) is for no-leak samples.

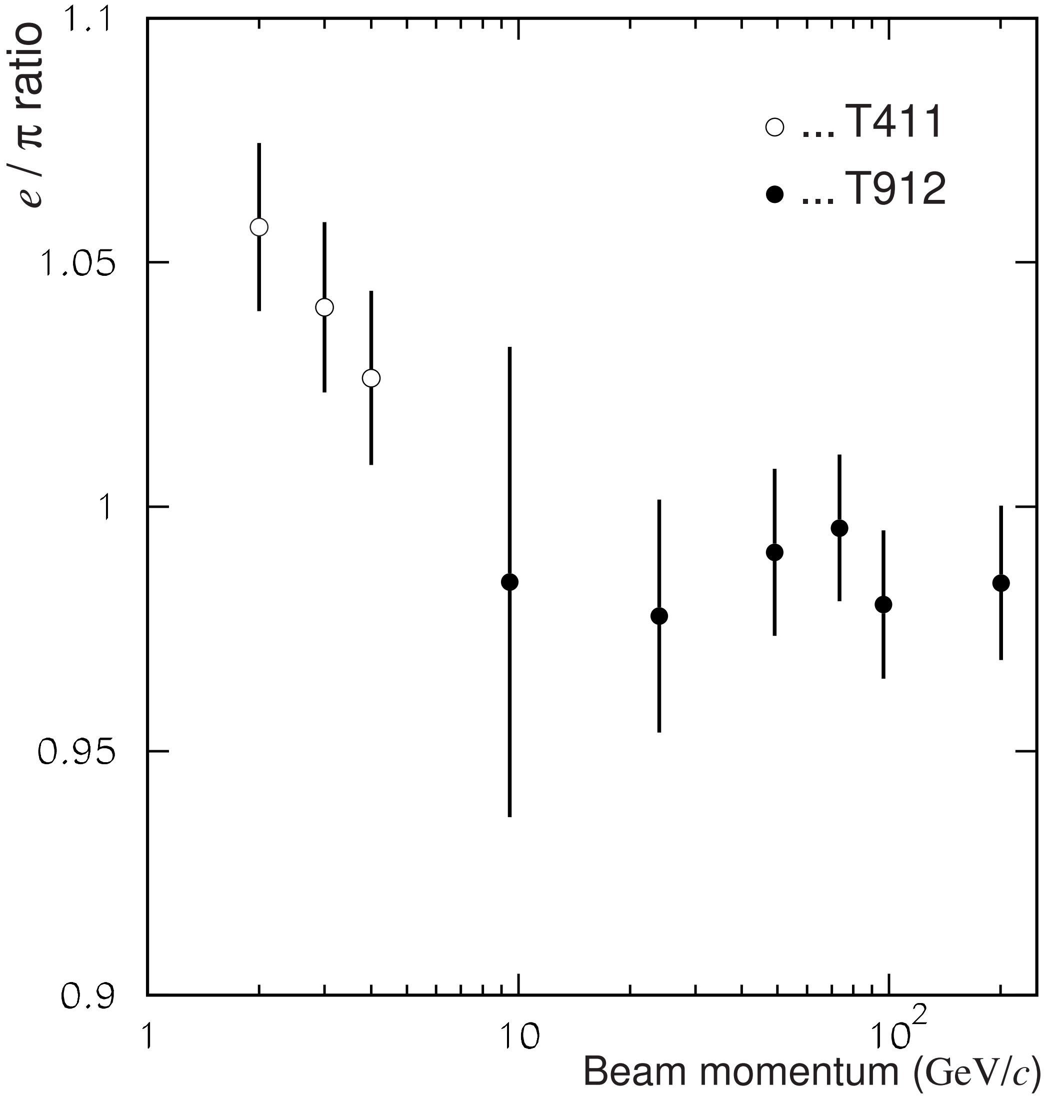

Fig. 22. e/π ratio of the calorimeter.